JOURNAL OF MATERIALS SCIENCE 37 (2002) 3573–3583

Effects of residual carbon content on sintering shrinkage, microstructure and mechanical properties of injection molded 17-4 PH stainless steel

YUNXIN WU, R. M. GERMAN, D. BLAINE, B. MARX, C. SCHLAEFER
Center for Innovative Sintered Products, P/M Lab, 147 Research West, The Pennsylvania State University, University Park, PA 16802-6809, USA
E-mail: rmg4@psu.edu

Carbon contamination from the thermoplastic binder is an inherent problem with the metal powder injection molding process. Residual carbon in the compacts after debinding has a strong impact on the sintering process, microstructure, and mechanical properties. In this study, injection molded 17-4 PH stainless steel was debound to two levels of residual carbon, 0.203 ± 0.014 wt% and 0.113 ± 0.008 wt%, by elevating the debinding temperature from 450°C to 600°C. Dilatometry in H_2 atmosphere shows that the 600°C-debound compacts shrink much faster than those debound at 450°C when the sintering temperature rises to over 1200°C. Density measurements for tensile bars sintered between 1260°C and 1380°C confirm the beneficial effect of low residual carbon content on sintering shrinkage. Quantitative metallography reveals that more δ-ferrite forms along austenite grain boundaries during sintering of the 600°C-debound compacts. In both samples, density gradients across the compact section are correlated with the residual carbon content and corresponding δ-ferrite formation. Finally, tensile tests show that the 600°C-debound compacts have lower tensile strength but higher ductility than those debound at 450°C. The relevant mechanisms are discussed with a focus on the effects of residual carbon content, δ-ferrite amount, and porosity.

1. Introduction

The alloy 17-4 PH is a precipitation-hardenable martensitic stainless steel. Due to its high strength and good corrosion resistance, 17-4 PH is widely used for medical, automotive, and aircraft components. Among various routes for manufacturing 17-4 PH components, metal powder injection molding (PIM) is most attractive, since it is a net-shape forming process with advantages of shape complexity, material utilization, and high final density [1].

The PIM process consists of four steps [2]: (1) preparation of feedstock by mixing alloy powder with a polymeric binder(s); (2) injection of feedstock into a mold to make an oversized preform; (3) thermal or solvent debinding to remove the majority of the polymer; and (4) sintering in a controlled atmosphere to densify the metal powder. Variation in the carbon content of the metal is often induced in the third step by either incomplete binder degradation or reaction between carbon and debinding gas [3]. Further variations may also be introduced in the early fourth step by carbon-oxygen and/or carbon-hydrogen reactions [4, 5]. Therefore, carbon control is a major issue associated with the injection molding of metals. In the case of injection molding of 17-4 PH, more attention should be paid to carbon control, because of the high sensitivity of the properties of this steel to the residual carbon content [6].

Earlier investigations on PIM 17-4 PH [1, 7–11] focused on the effects of powder characteristics, sintering atmosphere, sintering temperature, and heat treatment on the microstructure, and corresponding mechanical and corrosion properties. Until recently, little effort has been devoted to the effects of residual carbon content. Baba *et al.* [12] found that the residual carbon after sintering correlated to debound-state carbon contents. Further, the amount of retained austenite increased with an increase of the residual carbon content, resulting in an abrupt degradation of both hardness and tensile strength when the residual carbon content was over 0.1 wt%. Kyogoku *et al.* [13] confirmed that with increasing debinding temperature, the carbon content in both the debound compact and the sintered compact decreased continuously, and the sintered microstructures changed from austenite and martensite to martensite and delta (δ)-ferrite. More importantly, with increasing residual carbon content in the range 0.013 wt%–0.200 wt%, both the density and yield strength of the sintered compacts decreased, whereas the tensile strength increased. Unfortunately, no mechanistic explanation has been offered to describe

how the residual carbon content influences the sintering densification process with respect to microstructural evolution. In addition, the dependence of mechanical properties on residual carbon content seems to be controversial between Kyogoku *et al.* and Baba *et al.* Recent research by Newkirk *et al.* [5] and Green [14] preferred to use extremely low residual carbon levels (around 0.02 wt%), but no comparisons of sintering shrinkage and mechanical properties were provided.

The current study aims to correlate the sintering shrinkage, microstructure, and mechanical properties of PIM 17-4 PH with its residual carbon content. An emphasis is placed on the effects of δ-ferrite formation and its variation with both residual carbon content and sintering temperature on the sintering densification process. Dilatometry was performed to compare the sintering shrinkage behavior of the PIM compacts debound to different levels of residual carbon. Quantitative metallography was employed to measure the porosity and δ-ferrite content in the sintered tensile bars. In particular, cross-sectional gradients in porosity and δ-ferrite distribution were correlated with the carbon gradient. Finally, sintered tensile properties were evaluated in the H1100 heat treatment condition, and the fracture surfaces were analyzed under a scanning electron microscope.

2. Experimental procedures

The powder used for injection molding in this study was gas-atomized 17-4 PH stainless steel, with a tap density of 4400 kg/m^3 and a pycnometer density of 7690 kg/m^3. The particle size distribution of this powder is $D_{10} = 5$ μm, $D_{50} = 11$ μm, $D_{90} = 21$ μm. The chemical composition of the powder is given in Table I.

The powder was mixed with an agar-based binder, which is suitable for molding large, thick parts at significantly lower injection pressures than traditional PIM feedstocks [15]. The solids loading in the mixture was 55 vol%. The mixture was injection molded into tensile bars of 75.0 mm length, 7.6 mm width, 7.6 mm thickness, and 42.0 mm gauge section. Thermal debinding was performed in hydrogen using the following schedules: ramp at 2°C/min from room temperature to 450°C or 600°C with intermediate holds at 60°C for 2 h and 110°C for 1 h; hold at 450°C or 600°C for 2 h; cool down to room temperature at 5°C/min. The 450°C-debound PIM tensile bars had an average residual carbon content of 0.203 wt%, with a deviation of + 0.014 wt% in the center and −0.014 wt% at the surface; the 600°C-debound bars had an average residual carbon content of 0.130 wt%, with a deviation of + 0.008 wt% in center and −0.008 wt% at surface.

The sintering shrinkage behavior was evaluated with a vertical pushrod dilatometer. The samples were cut from the gauge length of the debound tensile bars, with a dimension of 13 mm in height, 7.6 mm in width, and 7.6 mm in thickness. Pure hydrogen was used as the sintering atmosphere, with an inlet dew point of −75°C. The dilatometry samples were sintered following the same cycle: heating to 1010°C at a rate of 10°C/min and holding at 1010°C for 1 h, then heating to 1380°C at a rate of 2°C/min and holding at 1380°C for 1 h, followed by cooling to room temperature at a rate of 10°C/min.

TABLE I Chemical composition of 17-4 PH stainless steel powder

Composition in weight percent (wt%)											
Fe	Cr	Cu	Ni	Nb + Ta	Mn	Si	C	S	O	N	
Bal.	16.7	4.0	4.5	0.29	0.12	0.45	0.031	0.001	0.095	0.029	

On the basis of dilatometry, five key points along the heating pathway, i.e., 1260°C, 1300°C, 1330°C, 1365°C, and 1380°C, were selected as peak temperatures for tensile bar sintering in a horizontal furnace. The sintering cycle and the atmosphere were the same as those used in the dilatometry study, except that the holding time at the peak temperatures was increased to 100 min in consideration of the enlarged sample size.

Densities of the sintered tensile bars were measured by the Archimedes (water immersion) method. The center of the gauge section was cut from one of the tensile bars in each sintering run: one half was used for residual carbon analysis, and another was mounted for cross-sectional microstructure examination. After being polished to 0.3 μm surface finish, the mounted samples were etched using a Kalling's reagent composed of 2 g $CuCl_2$, 40×10^{-6} m^3 HCl, 60×10^{-6} m^3 ethanol, and 40×10^{-6} m^3 H_2O. Optical quantitative metallography analysis was then carried out to measure the area fractions of the porosity and δ-ferrite across the tensile bar section. The optical microscope images were digitalized for image processing and quantification. A 200 times magnification was used for imaging, and at least five images were processed for each quantitative metric.

Finally, the sintered tensile bars were heat treated to H1100 condition through the following two steps: solution treatment—austenizing at 1038°C for 1 h in argon, followed by water quenching; aging—holding at 593°C for 4 h in argon, followed by air cooling. Tensile tests were performed to evaluate the mechanical properties of the heat-treated tensile bars. The fracture surfaces were examined using a scanning electron microscope (SEM).

3. Results

3.1. Sintering shrinkage

Fig. 1 plots the dilatometry data of sintering shrinkage and shrinkage rate versus temperature. As shown in Fig. 1a, the 600°C-debound sample has same shrinkage behavior as the 450°C-debound sample during heating from room temperature to 900°C. Below 630°C they are subject only to thermal expansion; from 630°C to 900°C, the thermal expansion is offset in part by a small amount of shrinkage that peaks around 740°C. Dramatic shrinkage starts at about 900°C for both samples, but the shrinkage behavior thereafter is influenced by the debinding condition.

Beginning from 900°C, the 600°C-debound sample shrinks slightly faster than the 450°C-debound sample, even during the 1 h hold at 1010°C. However, both debinding conditions give almost the same shrinkage around 1200°C, because the 600°C-debound sample

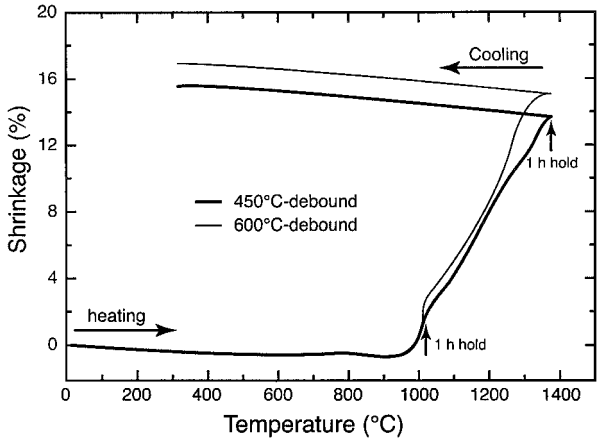

(a)

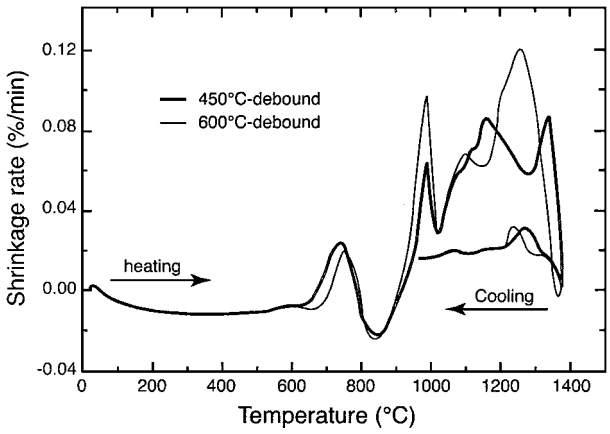

(b)

Figure 1 Dilatometry curves of PIM 17-4 PH showing the influence of debinding condition on sintering shrinkage. (a) Shrinkage versus temperature; (b) shrinkage rate versus temperature.

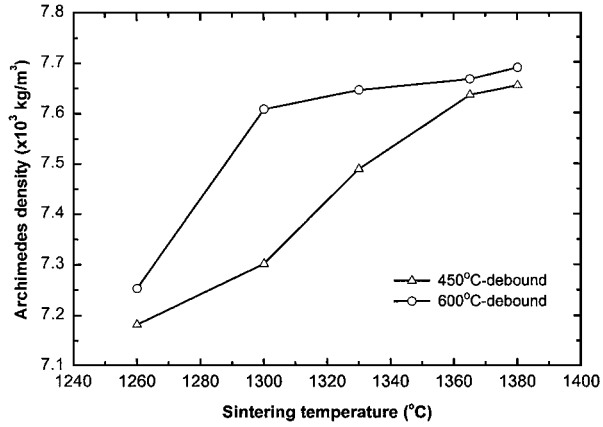

Figure 2 Archimedes densities of PIM 17-4 PH sintered at different temperatures.

decelerates its shrinkage around 1100°C, while the 450°C-debound sample accelerates continuously until 1160°C.

A remarkable difference in the shrinkage behavior is observed above 1200°C. The 600°C-debound sample shrinks much faster than the 450°C-debound sample, and its densification is completed much earlier around 1340°C. In comparison, the 450°C-debound sample decelerates its shrinkage until about 1300°C, above which acceleration in shrinkage occurs and densification continues till the 1 h hold at 1380°C. As a result, the 600°C-debound sample obtains a higher total sintering shrinkage. During subsequent cooling, both samples are subject to the same amount of thermal contraction.

The above shrinkage behavior can be better characterized by the variations in shrinkage rate. As displayed in Fig. 1b, both samples have four shrinkage rate peaks upon heating and one more shrinkage rate peak upon cooling. Positions of these peaks are listed in Table II. The positions of the first two peaks are not varied obviously with the debinding condition; however, the remaining three peaks shift noticeably to lower temperatures in the case of 600°C debinding. According to our previous work on the phase changes of water-atomized 17-4 PH during sintering [16], the shrinkage rate peak I is caused by the austenizing transformation $\alpha \rightarrow \gamma$; peak II is induced by deceleration of the heating ramp before the 1 h hold at 1010°C; peak III is an indication of the early intermediate stage of sintering; peak IV is related to δ-ferrite formation along austenite grain boundaries; and peak V is associated with the $\delta \rightarrow \gamma$ transformation. From the present dilatometry results, it can be inferred that the sintering densification process of PIM 17-4 PH has been promoted significantly by elevating the debinding temperature from 450°C to 600°C.

The densities of the sintered tensile bars further demonstrate the beneficial effect of 600°C debinding. As seen from Fig. 2, the 600°C-debound tensile bars obtain higher densities than the 450°C-debound tensile bars after sintering at the same temperatures ranging from 1260°C to 1380°C. For the 600°C-debound tensile bar, an abrupt increase in density occurs when the sintering temperature rises from 1260°C to 1300°C; for the 450°C-debound tensile bar, however, dramatic increase in density is postponed to higher temperatures in the range 1300°C to 1365°C. This difference agrees well with the dilatometry results shown in Fig. 1, indicating that shrinkage rate peak IV is responsible for fast densification of 17-4 PH in the later stages of sintering. The relevant mechanism and its relation to the residual carbon content and microstructure are analyzed in the following sections.

3.2. Microstructures

Microstructures of the sintered 17-4 PH tensile bars consist of three main constituents: pores, martensite, and δ-ferrite. Retained austenite may also be included but cannot be distinguished from martensite under an

TABLE II Positions of shrinkage rate peaks during sintering

Sample	Peak I	Peak II	Peak III	Peak IV	Peak V
450°C-debound	735–745°C	993°C	1158–1166°C	1332–1341°C	1261–1275°C
600°C-debound	752–755°C	991°C	1095–1105°C	1260–1267°C	1231–1245°C

optical microscope due to its small fractions. Both the porosity and the amount of δ-ferrite vary with the sintering temperature, and are greatly influenced by the debinding temperature and the residual carbon content. In addition, gradients in porosity and δ-ferrite distributions across the tensile bar sections exist. Fig. 3 compares the near-surface microstructures of the tensile bars sintered at different temperatures. The micrographs were taken from the sub-layers of the samples, which were about 1 mm below the surfaces. Fig. 4 shows the corresponding microstructures in the central areas of the samples. The porosity and δ-ferrite content measured by quantitative metallography are plotted in Fig. 5 as area fraction against sintering temperature.

When sintered to 1260°C, δ-ferrite (white in color) is formed at the surface of the 600°C-debound sample (Fig. 3a). The area fraction of δ-ferrite is measured as 0.69%, but the actual content would be higher during sintering, because some of the δ-ferrite transforms back to austenite upon cooling. It can be clearly seen that the δ-ferrite phase is preferentially precipitated at the austenite (transformed to martensite upon cooling below 220°C) grain boundaries. Along with the formation of δ-ferrite, most pores are spherical, especially for those situated at the grain boundaries, indicating the surface layer has reached the final stage of sintering [17]. In comparison, no δ-ferrite is formed in the center area of this sample, and most of the pores remain

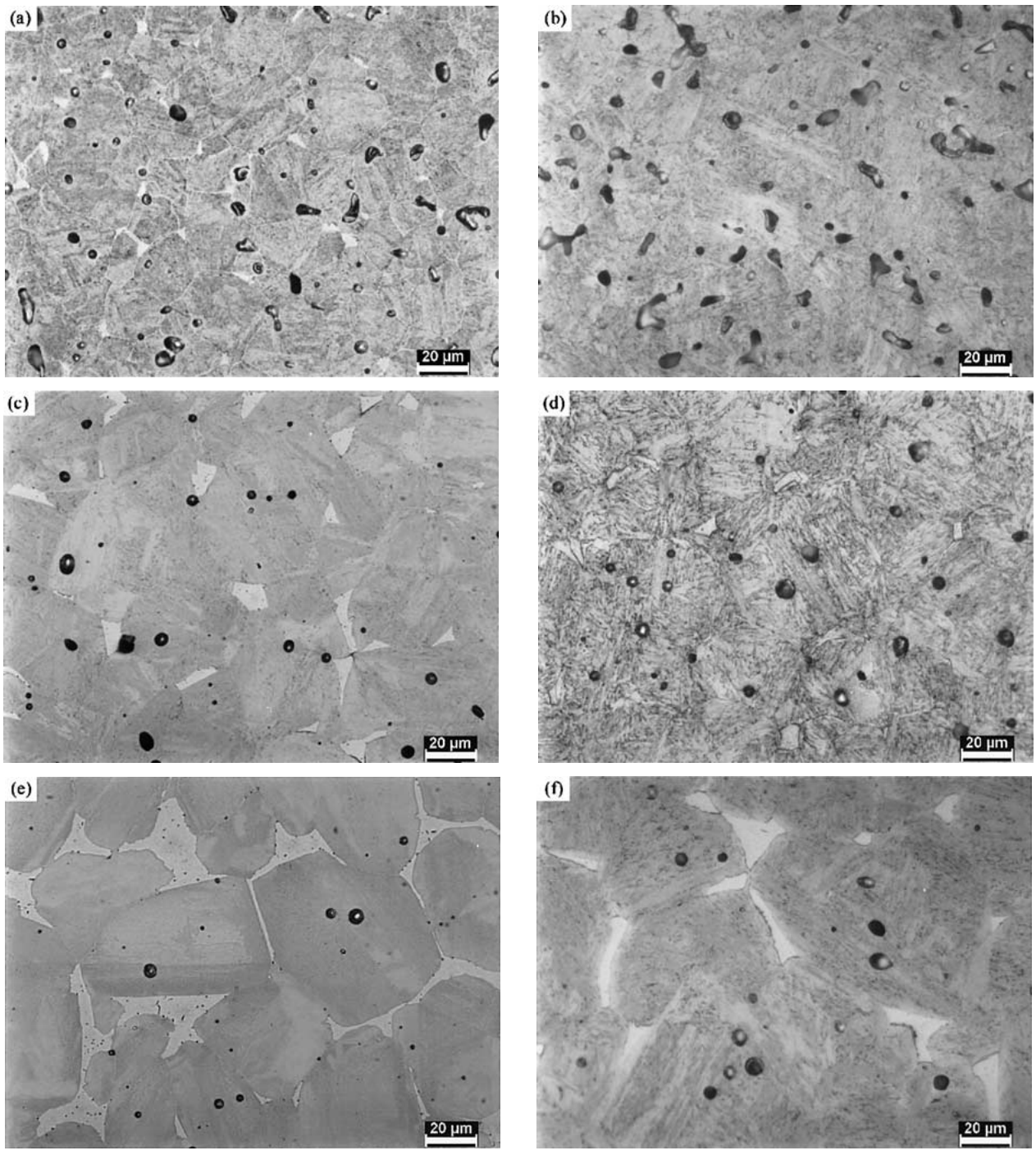

Figure 3 Near-surface microstructures of PIM 17-4 PH subjected to different debinding and sintering conditions. (a) 600°C-debound, 1260°C-sintered; (b) 450°C-debound, 1260°C-sintered; (c) 600°C-debound, 1330°C-sintered; (d) 450°C-debound, 1330°C-sintered; (e) 600°C-debound, 1380°C-sintered; (f) 450°C-debound, 1380°C-sintered.

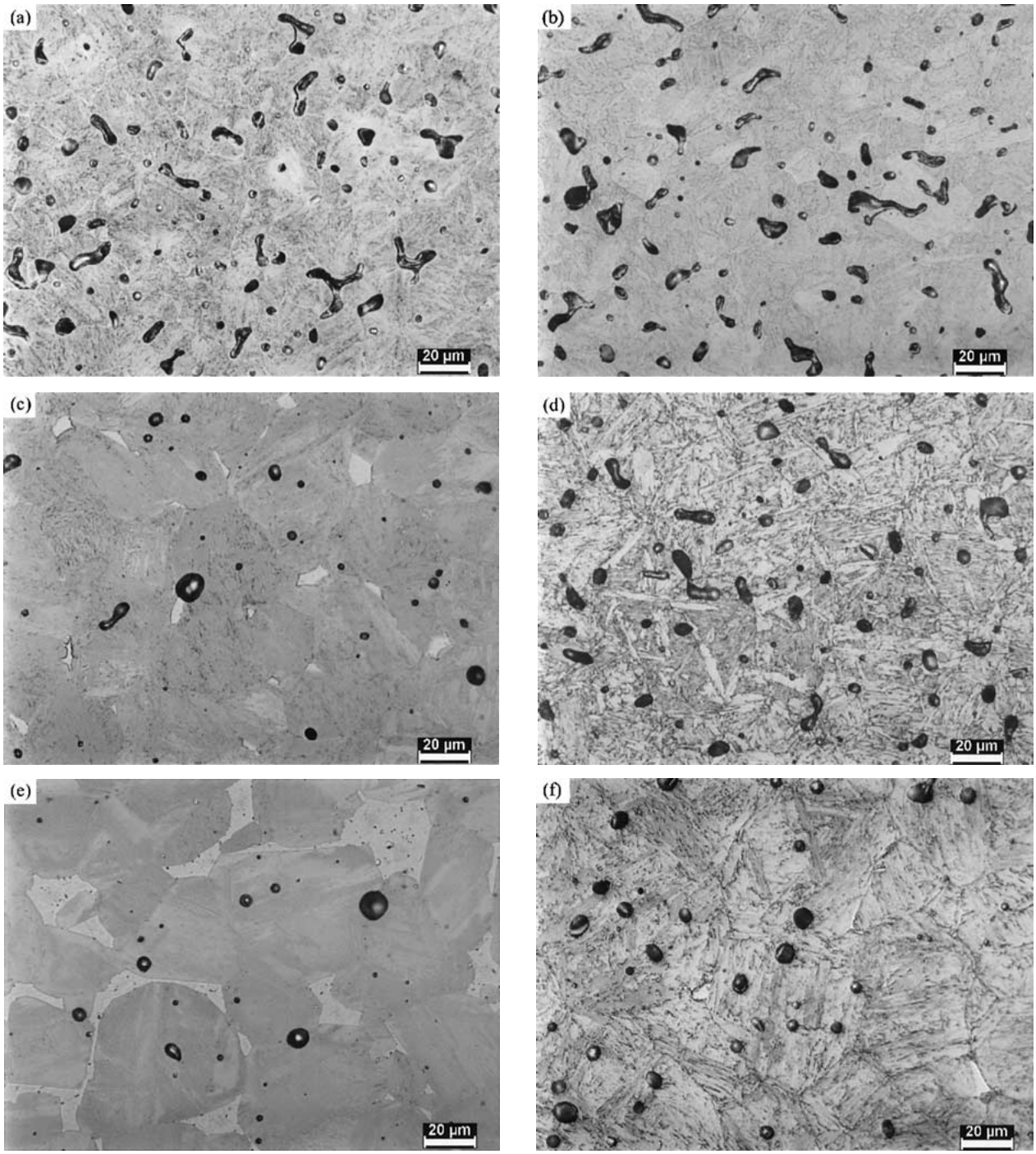

Figure 4 Microstructures in center areas of PIM 17-4 PH subjected to different debinding and sintering conditions. (a) 600°C-debound, 1260°C-sintered; (b) 450°C-debound, 1260°C-sintered; (c) 600°C-debound, 1330°C-sintered; (d) 450°C-debound, 1330°C-sintered; (e) 600°C-debound, 1380°C-sintered; (f) 450°C-debound, 1380°C-sintered.

unspheroidized (Fig. 4a). These differences indicate that a large porosity gradient is present across the sample section, as shown in Fig. 5a. In the case of 450°C debinding, no δ-ferrite has been formed after the 1260°C sintering (Figs 3b and 4b). The porosity at the surface is very close to that in the center, and the large, irregularly shaped pores imply that the sample is still in the intermediate stage of sintering, just like that shown in Fig. 4a.

When sintered to 1300°C, δ-ferrite increases to 2.29% at the surface of the 600°C-debound sample; meanwhile, 1.12% δ-ferrite has also been formed in the center (Fig. 5b). Consequently, there is an abrupt decrease in porosity (Fig. 5a). In contrast, there is still no measurable δ-ferrite in the 450°C-debound sample, and the porosity is much higher. However, Fig. 5a reveals a faster decrease in porosity at the sample surface, as compared to the center. This means that a small amount of δ-ferrite could have formed at the surface during sintering at 1300°C, but was transformed to austenite on cooling.

With increasing sintering temperature to 1330°C, δ-ferrite increases to 2.69% at the surface and to 1.31% in the center for the 600°C-debound sample; meanwhile, the reduction in porosity continues, but with a decreased rate (Fig. 5a). As shown in Figs 3c and 4c, almost all the remaining pores have spheroidized and shrunk to much smaller sizes, and most are located

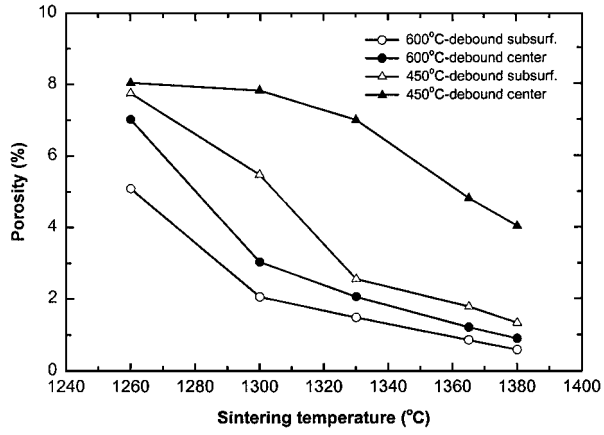

(a)

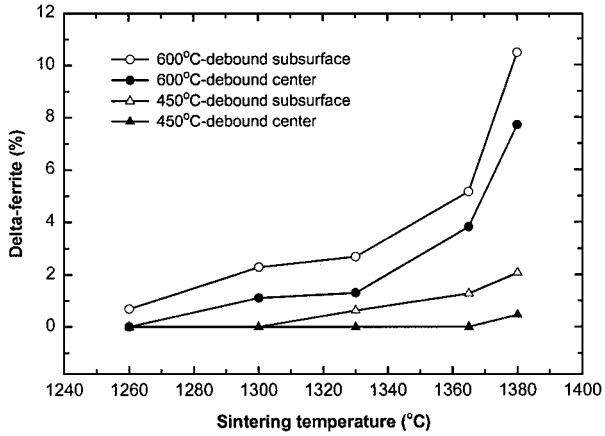

(b)

Figure 5 Variations in cross-sectional porosity (a) and δ-ferrite content, (b) of PIM 17-4 PH with sintering temperature.

inside the original austenite grains, away from the δ-ferrite. Moreover, the porosity gradient across the section is reduced considerably if compared with the 1260°C sintering. On the contrary, the porosity gradient is enlarged in the 450°C-debound sample, because of the formation of δ-ferrite at its surface. As shown in Fig. 3d, δ-ferrite precipitates along the grain boundaries, very similar to that shown in Fig. 3a. The pores are becoming spherical, but the pore sizes are still larger than those shown in Fig. 3c. In the center area of the sample, there is still no δ-ferrite formed, and most of the pores remain unspheroidized (Fig. 4d).

Further increasing the sintering temperature, δ-ferrite increases more rapidly in the 600°C-debound sample, but porosity decreases at almost the same rate as before, since nearly full densification has been reached (Fig. 5). After sintering at 1380°C, the δ-ferrite content is measured as 10.48% at the surface and 7.71% in the center. As seen from Figs 3e and 4e, δ-ferrite tends to form a network along the original austenite grain boundaries, and the remaining small pores are all located inside the austenite grains. In addition, the porosity across the section becomes much more uniform. For the 450°C-debound sample, δ-ferrite begins to form above 1330°C in the center area. After sintering at 1380°C, the δ-ferrite content reaches 2.07% at the surface, and the pores are spheroidized (Fig. 3f). Moreover, 0.46% δ-ferrite is precipitated along grain boundaries in the center (Fig. 4f), resulting in a dramatic decrease in porosity, as shown in Fig. 5a. However, the overall porosity of the 450°C-debound sample is higher and the porosity gradient is larger than that of the 600°C-debound sample.

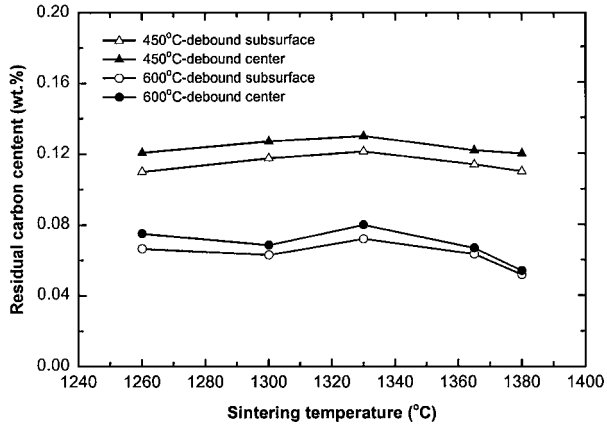

Figure 6 Residual carbon contents of sintered PIM 17-4 PH.

The cross-sectional microstructural gradients and their difference between the 600°C- and 450°C-debound samples can be correlated with the sintered-state residual carbon contents. As shown in Fig. 6, the 450°C-debound samples have a residual carbon content of 0.120 ± 0.012 wt% after sintering, whereas the 600°C-debound samples obtain a much lower residual carbon content of 0.060 ± 0.010 wt%. In addition, the cross-sectional gradient in the residual carbon content still exists in both kinds of samples. In accordance with their debound-state carbon gradients, the sintered 450°C-debound samples have a larger cross-sectional carbon gradient than the sintered 600°C-debound samples. With increasing temperature between 1260°C and 1380°C, the residual carbon content does not change significantly. This means that decarburization of the debound PIM compacts occurs mainly in the early stages of sintering, favored by the open pore structures [5]. Relationships among the residual carbon content, δ-ferrite formation, and pore shrinkage are discussed later in this paper.

The tensile bars that are heat-treated to H1100 condition consist of tempered martensite, δ-ferrite, and pores. Compared with the sintered-state, there is no measurable change to the porosity after heat treatment, but the morphology of δ-ferrite is altered. As seen from Fig. 7, the edges of the δ-ferrite regions become dull, and the network-like structure changes to a more discrete morphology, as a result of the solution treatment. Quantitative metallography shows that about 1% of δ-ferrite dissolves during the 1 h austenization at 1038°C. In 17-4 PH, a discrete δ-ferrite morphology is required to improve its ductility, strength, and toughness [10].

3.3. Mechanical properties

Fig. 8 shows the variations in both tensile strength and elongation of the tensile bars after H1100 heat treatment, as a function of sintering temperature. It can be found that the 450°C-debound tensile bars have higher tensile strength but lower elongation than the 600°C-debound tensile bars. Moreover, with increasing sintering temperature, the tensile strength peaks at 1365°C

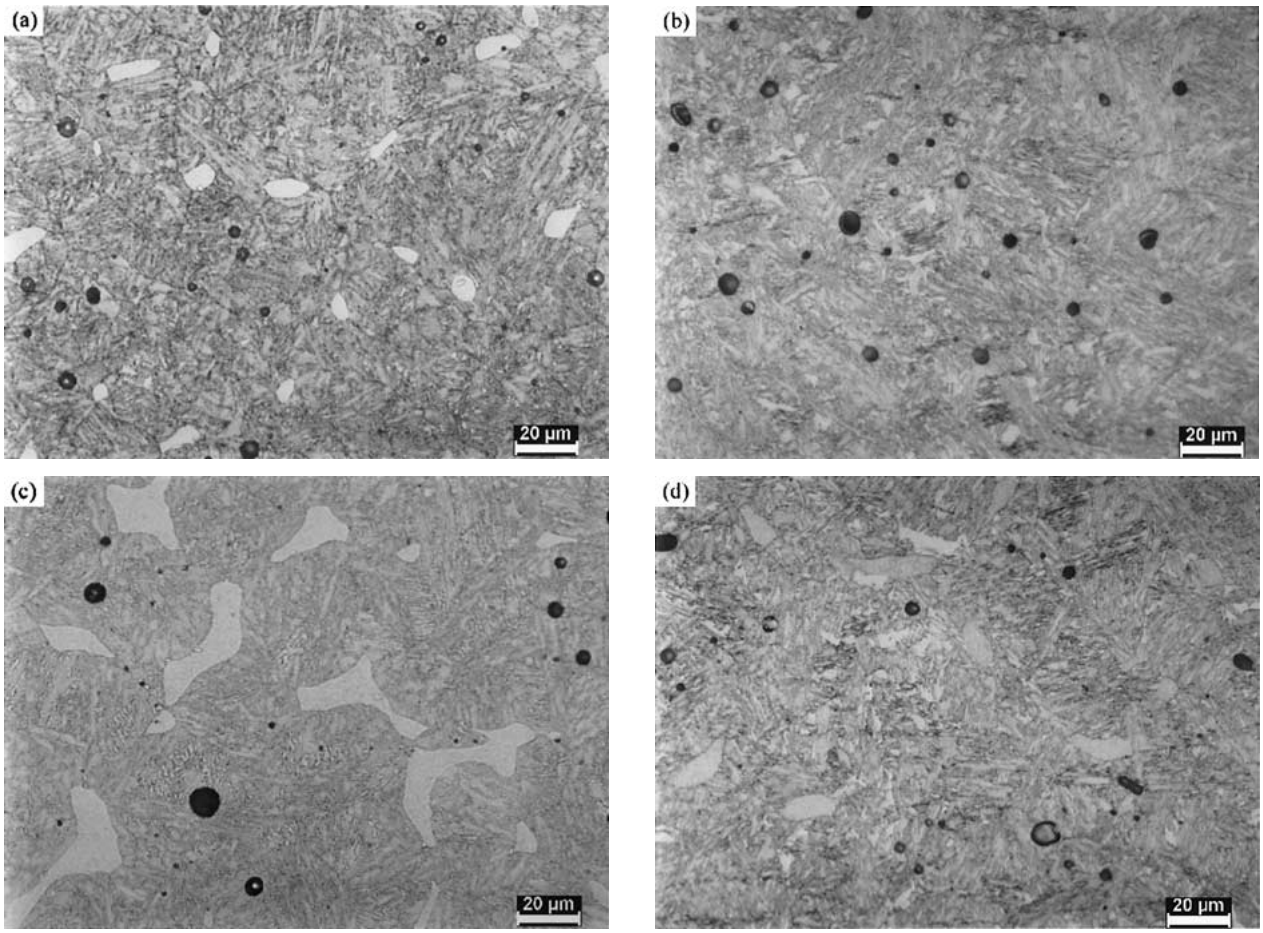

Figure 7 Near-surface microstructures of PIM 17-4 PH in H1100 heat treatment condition. (a) 600°C-debound, 1330°C-sintered; (b) 450°C-debound, 1330°C-sintered; (c) 600°C-debound, 1380°C-sintered; (d) 450°C-debound, 1380°C-sintered.

for the 450°C-debound samples and at 1330°C for the 600°C-debound samples. This means that the tensile strength of the sintered 17-4 PH is not only determined by the residual carbon content, as revealed by Kyogoku *et al.* [13], but also depends on the sintering temperature. With increasing sintering temperature, the compacts are densified with continuous decrease in porosity; meanwhile, the δ-ferrite content increases, resulting in a reduction in the martensite content. By combining the δ-ferrite data shown in Fig. 5b with the tensile strength variation shown in Fig. 8a, it can be inferred that the tensile strength is obviously degraded when the δ-ferrite content is above 2% or so.

In comparison, the ductility of the sintered 17-4 PH is not adversely influenced by the δ-ferrite content. The lower the residual carbon content, the higher the elongation. In addition, elongation increases continuously with increasing sintering temperature. Fig. 9 shows the morphologies of the tensile fracture surfaces. It can be seen that all the samples exhibit dimpled rupture, but the dimple morphology varies with the debinding and sintering conditions. For the 1330°C sintered 450°C-debound tensile bar, most of the dimples have a large size around 10 μm (Fig. 9a). When the sintering temperature rises to 1380°C, the large-sized dimples are reduced remarkably, and most of the dimples are smaller than 5 μm (Fig. 9b). The increase in the small-sized dimples corresponds to the improvement in ductility as shown in Fig. 8b. For the 600°C-debound tensile bars, there are a larger amount of small-sized dimples on the fracture surfaces (Fig. 9c and d), correlating higher ductility with the high temperature debinding.

In consideration of the microstructural difference across the tensile bar section, the morphology of the outer area on the fracture surface is also examined and shown in Fig. 9e and f. Compared to the center area shown in Fig. 9d, the fracture surface in the outer area is much smoother, because of the lack of large, deep dimples. Extremely small dimples with sizes less than 1 μm occupy most of the outer area, and the remaining large dimples are usually shallow. The magnified image in Fig. 9f shows that the shallow dimples are located at the δ-ferrite regions. Neither microcracks nor brittle rupture is found with the δ-ferrite. Therefore, δ-ferrite does not show any adverse effect on ductility in this paper. Based on the fact that the large dimples on the fracture surfaces have very similar sizes and distributions to the pores shown in Figs 3 and 4, it can be drawn that the large dimples are initiated predominantly at the pores; thus, the ductility of the sintered 17-4 PH depends mainly on the porosity.

4. Discussion

4.1. Relation between residual carbon content and δ-ferrite formation

When sintered, 17-4 PH stainless steel has a two-phase microstructure consisting of a mixture of δ-ferrite and martensite. According to the Schaeffler constitution diagram of stainless steel [6], the fraction of δ-ferrite in the mixture varies with the Ni equivalent and Cr

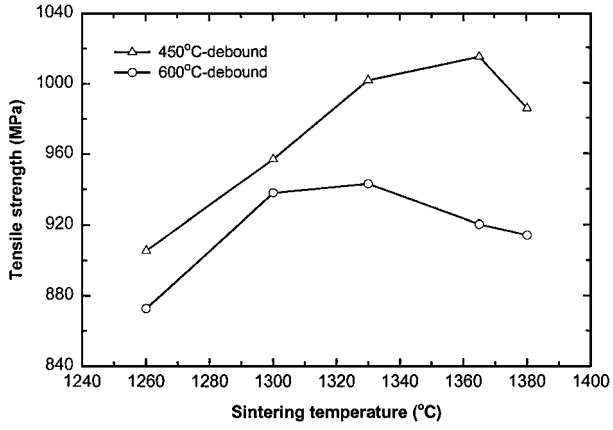

(a)

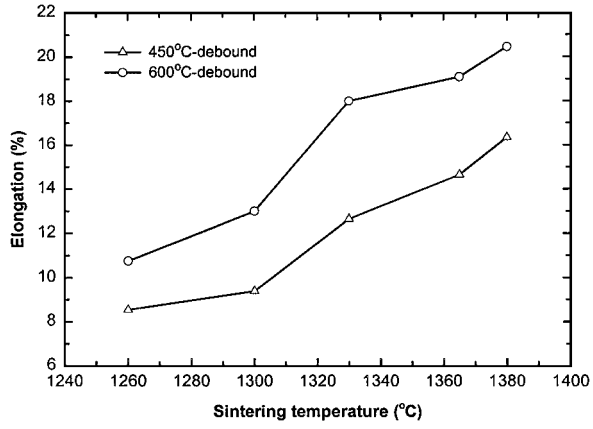

(b)

Figure 8 Tensile properties of PIM 17-4 PH in H1100 heat treatment condition. (a) Tensile strength; (b) elongation.

equivalent. Carbon is a major contributor to the Ni equivalent. The lower the carbon content, the higher the δ-ferrite fraction. For investigations on the sintering process of PIM 17-4 PH, information about the δ-ferrite content is important. Unfortunately, there is no diagram describing accurately the variation in δ-ferrite content with sintering temperature and residual carbon content.

The ternary iron-chromium-carbon constitution diagram at 13% Cr [6] is shown in Fig. 10 as a reference phase diagram. It is expected that the γ phase region shown in this diagram is enlarged for 17-4 PH due to the existence of 4.5% Ni. According to the diagram, 17-4 PH experiences the following sequential solid-state phase changes during heating: $\alpha + C_1(M_{23}C_6) \rightarrow \alpha + \gamma + C_1 \rightarrow \gamma \rightarrow \gamma + \delta \rightarrow \delta$. The exact temperatures of these phase changes may vary with the composition and the heating rate. In this work, the $\alpha \rightarrow \gamma$ transformation occurs around 740°C, resulting in a small amount of shrinkage (Peak I) due to the difference in atomic packing density between the BCC-structured α and FCC-structured γ. The diagram also shows that the starting temperature for $\gamma \rightarrow \gamma + \delta$ transformation varies largely with the carbon content. The lower the carbon content, the lower the starting temperature. The present paper shows that when sintered between 1260°C and 1380°C, the 450°C-debound PIM 17-4 PH has higher residual carbon content than the 600°C-debound sample (0.120 ± 0.012 wt% and 0.060 ± 0.010 wt%, respectively). Consequently, δ-ferrite begins to form at around 1300°C in the former, whereas 0.69% δ-ferrite has been formed at 1260°C in the latter. With increasing sintering temperature, the amount of δ-ferrite increases in both samples, but the 600°C-debound sample has a higher δ-ferrite content than the 450°C-debound sample. In addition, due to the carbon gradient across the section, δ-ferrite is not uniformly distributed in the samples, with a higher content at surface and a lower in the center.

4.2. Role of δ-ferrite in sintering densification

Dilatometry and microstructural analysis revealed that a high shrinkage rate (Peak IV) occurs when δ-ferrite begins to form during sintering. Low residual carbon content lowers the starting temperature of $\gamma \rightarrow \delta$ transformation significantly, thus promoting the densification of PIM 17-4 PH. The density measurement as well as the cross-sectional porosity analysis for the sintered tensile bars further confirms the beneficial effect of δ-ferrite on sintering densification.

The role of δ-ferrite in sintering densification of 17-4 PH can be analyzed on the basis of sintering kinetics. In general, during the intermediate stage of sintering, stainless steels densify mainly by grain boundary diffusion due to its lower activation energy as compared to volume (lattice) diffusion [17]. Vacancies from the pores at the interparticle junctions migrate along the grain boundaries, and are annihilated there, giving a reverse flow of mass from the grain boundary to the pore surface. Any change to the mass-transport process would affect the shrinkage rate. For 17-4 PH, the mass transport prior to δ-ferrite formation proceeds dominantly along the austenite grain boundaries. When δ-ferrite precipitates at the austenite grain boundaries and intersects with the pore surface, the mass-transport mechanism will be changed. First, the δ/γ interphase boundaries contribute to the mass transport, because they also act as the interfacial vacancy sink [17]. Second, δ-ferrite volume diffusion is very appreciable, because the coefficient of the volume diffusion in ferrite is generally one or two orders of magnitude higher than that in austenite [18], owing to its lower atomic packing density. Therefore, in the presence of δ-ferrite, the overall atomic diffusivity would be significantly increased, and more mass can be transported to the pore surface per unit time, thus resulting in a rapid pore shrinkage accompanied by an increased shrinkage rate and fast densification.

The beneficial effect of δ-ferrite exists also in the sintering of duplex stainless steels. Kamada *et al.* [19] and Puscas *et al.* [20] found that the shrinkage increased with an increase in the amount of δ-ferrite powder, because of the activated sintering by the high atomic diffusivity in δ-ferrite. Recent work by Datta *et al.* [21] further denoted that the enhanced sinterability by ferritic powder addition varied with the sintering temperature. Therefore, promoted sintering in the δ-ferrite containing alloy systems can be realized by manipulating the δ-ferrite content and the sintering temperature.

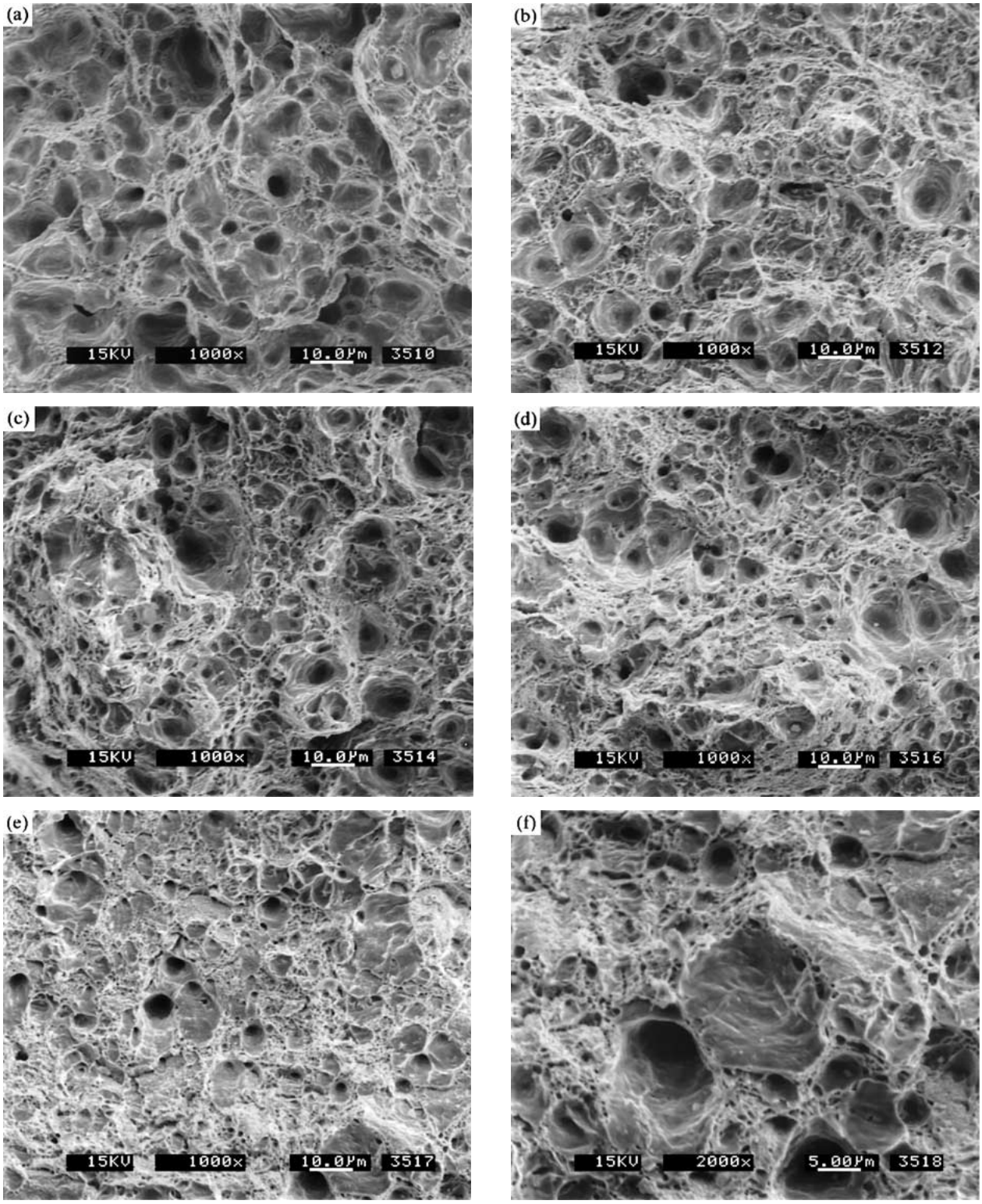

Figure 9 Fracture surface morphologies of PIM 17-4 PH tensile bars. (a) 450°C-debound, 1330°C-sintered, center; (b) 450°C-debound, 1380°C-sintered, center; (c) 600°C-debound, 1330°C-sintered, center; (d) 600°C-debound, 1380°C-sintered, center; (e) 600°C-debound, 1380°C-sintered, near surface; (f) high magnification of (e).

4.3. Effects of residual carbon content, δ-ferrite and porosity on tensile properties

The mechanical properties of the sintered PIM 17-4 PH are determined by the microstructures, which consist mainly of martensite, δ-ferrite, and porosity. The residual carbon content can influence not only the mechanical properties of martensite itself, but also the fractions of martensite and δ-ferrite. In general, an increase in martensite fraction, which means a decrease in ferrite fraction, results in an increase in tensile strength [22]. This is the reason why the 450°C-debound sample exhibits higher tensile strength than the 600°C-debound sample after sintering at the same temperatures. However, the porosity also plays an important role in the tensile behavior. As evident from above sections, the porosity decreases in both samples with increasing sintering temperature. As a result, the tensile strength increases until the δ-ferrite content rises to over 2.0% or so. This result helps to explain the phenomenon,

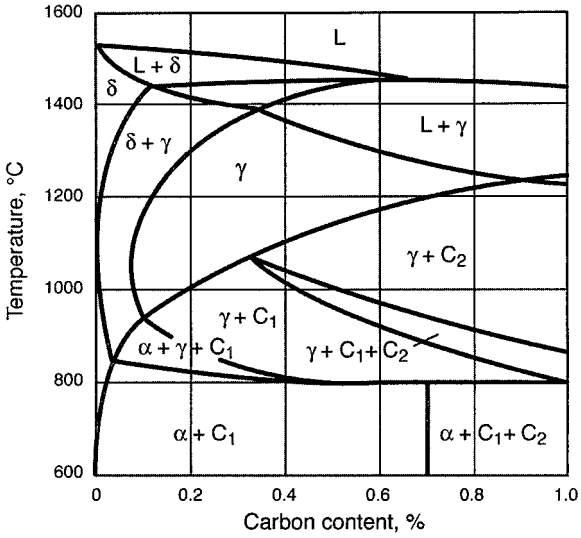

Figure 10 A ternary iron-chromium-carbon constitution diagram at 13% Cr [6].

found by Baba *et al.* [12] and Kyogoku *et al.* [13], that an abrupt decrease in tensile strength occurred at high residual carbon levels, which they ascribed to the effect of retained austenite. As for the ductility, the porosity appears to be more influential than the δ-ferrite content, as evident from the fracture morphologies shown in Fig. 9. The presence of pores favors the large-sized dimple rupture, thus lowering the ductility [13]. An empirical equation has been derived by German [23], with regard to the relation between the porosity and relative ductility of P/M materials. Nevertheless, an adverse effect of δ-ferrite on ductility would be seen if an extremely high content of δ-ferrite, e.g., above 16%, is involved [11].

Overall, the present paper shows that the mechanical properties of the sintered PIM 17-4 PH can be manipulated by controlling the debinding condition, residual carbon content, and the sintering temperature. Through subsequent heat treatment, the tensile strength and the ductility can be further adjusted to be comparable to those of the wrought 17-4 PH [24].

5. Conclusions

The effects of the residual carbon content after debinding on the sintering shrinkage behavior, microstructure, and mechanical properties of PIM 17-4 PH are closely related to the δ-ferrite phase formed during sintering. δ-ferrite precipitates along the austenite grain boundaries, and promotes densification. Therefore, a high shrinkage rate is induced by the formation of δ-ferrite during the intermediate state of sintering. Higher temperature debinding produces a lower residual carbon content, which favors the formation of δ-ferrite and a higher final density. Moreover, porosity gradients can be caused by the residual carbon gradient across the compact section. Compared with center area, surface layers of the compact possess less porosity, owing to their lower residual carbon contents and higher δ-ferrite contents. δ-ferrite decreases the tensile strength by reducing the fraction of martensite in the sintered structure, but helps to improve the ductility by decreasing the porosity.

Acknowledgments

The financial support from NIST/ATP Program "Powder Metal Injection Molding" under Grant No. 70NANBOH3019 is greatly acknowledged. The authors are grateful to James Stevenson and Jon Peltier, Honeywell Laboratories, Morristown, NJ, for providing PIM samples and helpful discussions on microstructure evolution. Thanks also go to Don Whychell, CM Furnaces, Bloomfield, NJ, and Jerry LaSalle, Polymer Technologies Inc., Clifton, NJ, for help in refining the sintering cycle. Help with heat treatment and SEM analysis from Timothy Mueller and Pavan Suri, P/M Lab, The Pennsylvania State University, is much appreciated as well.

References

1. R. M. GERMAN and D. KUBISH, *Int. J. Powder Metall.* **29** (1993) 47.
2. R. M. GERMAN and A. BOSE, in "Injection Molding of Metals and Ceramics" (Metal Powder Industries Federation, Princeton, New Jersey, 1997) p. 11.
3. M. A. PHILLIPS, E. L. STREICHER, M. RENOWDEN, R. M. GERMAN and J. M. FRIEDT, in Proceedings of the 1992 Powder Injection Molding Symposium, San Francisco, June 1992, edited by P. H. Booker, J. Gaspervich and R. M. German (Metal Powder Industries Federation, Princeton, New Jersey, 1992) p. 371.
4. H. OHTSUBO, K. MARUTA, K. NISHIMURA and Y. MAKIISHI, in Proceedings of the 1992 Powder Injection Molding Symposium, San Francisco, June 1992, edited by P. H. Booker, J. Gaspervich and R. M. German (Metal Powder Industries Federation, Princeton, New Jersey, 1992) p. 409.
5. J. W. NEWKIRK, J. A. SAGO and G. M. BRASEL, in "Processing and Fabrication of Advanced Materials," Vol. VII (The Minerals, Metals and Materials Society, Warrendale, PA, 1998) p. 213.
6. J. R. DAVIS, in "Stainless Steels" (ASM International, Materials Park, Ohio, 1994) p. 13.
7. R. T. FOX, D. LEE, M. K. BULGER and R. M. GERMAN, in "Advances in Powder Metallurgy," Vol. 3 (Metal Powder Industries Federation, Princeton, New Jersey, 1990) p. 359.
8. H. ZHANG and R. M. GERMAN, in Proceedings of the 1992 Powder Injection Molding Symposium, San Francisco, June 1992, edited by P. H. Booker, J. Gaspervich and R. M. German (Metal Powder Industries Federation, Princeton, New Jersey, 1992) p. 219.
9. S. BANERJEE, in Proceedings of the 1992 Powder Injection Molding Symposium, San Francisco, June 1992, edited by P. H. Booker, J. Gaspervich and R. M. German (Metal Powder Industries Federation, Princeton, New Jersey, 1992) p. 181.
10. J. J. VALENCIA, T. J. McCABE and H. DONG, in "Advances in Powder Metallurgy and Particulate Materials," Vol. 2 (Metal Powder Industries Federation, Princeton, New Jersey, 1995) p. 6.
11. J. J. VALENCIA and J. R. SPIRKO, in "Advanced Particulate Materials and Processes" (Metal Powder Industries Federation, Princeton, New Jersey, 1997) p. 411.
12. T. BABA, H. MIURA, T. HONDA and Y. TOKUYAMA, in "Advances in Powder Metallurgy and Particulate Materials," Vol. 2 (Metal Powder Industries Federation, Princeton, New Jersey, 1995) p. 6.
13. H. KYOGOKU, S. KOMATSU, H. NAKAYAMA, H. JINUSHI and K. SHINOHARA, in "Advances in Powder Metallurgy and Particulate Materials," Vol. 3 (Metal Powder Industries Federation, Princeton, New Jersey, 1997) p. 18.
14. K. A. GREEN, in "Advances in Powder Metallurgy and Particulate Materials," Vol. 2 (Metal Powder Industries Federation, Princeton, New Jersey, 1998) p. 5.
15. J. C. LASALLE and M. ZEDALIS, *JOM—J MIN MET MAT S* **51** (1999) 38.
16. Y. WU, D. BLAINE, B. MARX, C. SCHLAEFER and R. M. GERMAN, *Metall. Mater. Trans.* **33A**, in press.

17. R. M. GERMAN, in "Sintering Theory and Practice" (Wiley, New York, 1996) p. 68.
18. I. KAUR, W. GUST and L. KOZMA, in "Handbook of Grain and Interphase Boundary Diffusion Data" (Ziegler Press, Stuttgart, 1989) p. 536.
19. M. KAMADA and Y. TOKUNAGA, *J. Jpn. I. Met.* **55** (1991) 887.
20. T. M. PUSCAS, A. MOLINARI, J. KAZIOR, T. PIECZONKA and M. NYKIEL, *Powder Metall.* **44** (2001) 48.
21. P. DATTA and G. S. UPADHYAYA, *Mater. Chem. Phys.* **67** (2001) 234.
22. A. BAG and K. K. RAY, *Metall. Mater. Trans.* **32A** (2001) 2400.
23. R. M. GERMAN, in "Powder Metallurgy Science" (Metal Powder Industries Federation, Princeton, New Jersey, 1994) p. 383.
24. J. M. HOLT, H. MINDLIN and C. Y. HO, in "Structural Alloys Handbook," Vol. 2 (CINDAS/Purdue University, West Lafayette, Indiana, 1996) p. 6.

Received 26 November 2001
and accepted 6 May 2002